The collection 6 MODIS active fire detection algorithm and fire products

Louis Giglio[*], **Wilfrid Schroeder**, and **Christopher O. Justice**

Department of Geographical Sciences, University of Maryland, College Park, MD, USA

Abstract

The two Moderate Resolution Imaging Spectroradiometer (MODIS) instruments, on-board NASA's Terra and Aqua satellites, have provided more than a decade of global fire data. Here we describe improvements made to the fire detection algorithm and swath-level product that were implemented as part of the Collection 6 land-product reprocessing, which commenced in May 2015. The updated algorithm is intended to address limitations observed with the previous Collection 5 fire product, notably the occurrence of false alarms caused by small forest clearings, and the omission of large fires obscured by thick smoke. Processing was also expanded to oceans and other large water bodies to facilitate monitoring of offshore gas flaring. Additionally, fire radiative power (FRP) is now retrieved using a radiance-based approach, generally decreasing FRP for all but the comparatively small fraction of high intensity fire pixels. We performed a Stage-3 validation of the Collection 5 and Collection 6 Terra MODIS fire products using reference fire maps derived from more than 2500 high-resolution Advanced Spaceborne Thermal Emission and Reflection Radiometer (ASTER) images. Our results indicated targeted improvements in the performance of the Collection 6 active fire detection algorithm compared to Collection 5, with reduced omission errors over large fires, and reduced false alarm rates in tropical ecosystems. Overall, the MOD14 Collection 6 daytime global commission error was 1.2%, compared to 2.4% in Collection 5. Regionally, the probability of detection for Collection 6 exhibited a ~3% absolute increase in Boreal North America and Boreal Asia compared to Collection 5, a ~1% absolute increase in Equatorial Asia and Central Asia, a ~1% absolute decrease in South America above the Equator, and little or no change in the remaining regions considered. Not unexpectedly, the observed variability in the probability of detection was strongly driven by regional differences in fire size. Overall, there was a net improvement in Collection 6 algorithm performance globally.

Keywords

[*]Corresponding author at: Department of Geographical Sciences, University of Maryland, 2181 LeFrak Hall, College Park, MD 20742, USA.

1. Introduction

NASA's Moderate Resolution Imaging Spectroradiometer (MODIS) active fire products (Justice et al., 2002) were the first in a family of remotely sensed fire data sets produced from a new generation of moderate resolution (~1 km), "fire-capable" sensors on-board terrestrial satellites. Since their inception in 2000, the MODIS fire products have been used to help answer a broad range of scientific questions concerning the role of biomass burning within the Earth system (e.g. Chen, Velicogna, Famiglietti, & Randerson, 2013; Chuvieco, Giglio, & Justice, 2008; Ichoku & Kaufman, 2005; McCarty, Justice, & Korontzi, 2007; Mollicone, Eva, & Achard, 2006; Peterson, Hyer, & Wang, 2014; Vadrevu et al., 2012; Wooster & Zhang, 2004), and in numerous operational applications (e.g. Kaiser et al., 2012; Longo et al., 2010; Reid et al., 2009; Ressl et al., 2009; Sofiev et al., 2009; Wiedinmyer et al., 2011). The products have been found to have utility in the context of social and cultural analyses as well (e.g. Bromley, 2010; Koren, Remer, & Longo, 2007; Schroeder, Giglio, & Aravéquia, 2009).

A key element of NASA's Earth Observing System (EOS) mission is the capability to periodically reprocess the raw instrument data archive, using updated calibration and geolocation information, as well as the derived products (Justice et al., 2002). Reprocessing is an essential requirement for producing consistent, science quality data sets suitable for long-term monitoring of both regional and global change. As part of the EOS, most of the MODIS land products have been reprocessed periodically to implement algorithm changes and refinements. Here we describe improvements made to the active fire detection algorithm, and the associated MOD14 (Terra) and MYD14 (Aqua) fire products, for Collection 6, which represents the fourth major reprocessing of the MODIS time series. The Collection 6 algorithm is intended to address limitations observed with the previous Collection 5 fire product, notably the occurrence of false alarms arising from small forest clearings, and the omission of large fires obscured by thick smoke (Schroeder et al., 2008). Processing was also expanded to oceans and other large water bodies to facilitate monitoring of offshore gas flaring. We begin by briefly summarizing the status of the Collection 5 active fire products in Section 2. In Section 3, we describe the Collection 6 algorithm, emphasizing those aspects that have changed since Collection 5. In Section 4, we present a rigorous validation of both the Collection 5 and Collection 6 Terra MODIS fire product using a large sample of coincident, high resolution imagery from the Advanced Spaceborne Thermal Emission and Reflection Radiometer (ASTER).

2. Collection 5 product and algorithm status

Production of the Collection 5 MODIS fire products commenced in mid-2006. Since then, the products have been evaluated in a number of independent studies (e.g., Csiszar, Morisette, & Giglio, 2006; de Klerk, 2008; Freeborn, Wooster, & Roberts, 2010; Hantson, Padilla, Corti, & Chuvieco, 2013; Hawbaker, Radeloff, Syphard, Zhu, & Stewart, 2008; He & Li, 2011; Maier, Russell-Smith, Edwards, & Yates, 2013; Schroeder et al., 2008; Tanpipat, Honda, & Nuchaiya, 2009), and in the context of optimizing the global MODIS algorithm for use within a specific region (e.g. Cheng, Rogan, Schneider, & Cochrane, 2013; Ressl et al., 2009; Wang, Qu, Hao, Liu, & Sommers, 2007). A finding common to many of these

studies is that the global thresholds used to narrow the search for fire pixels (the "potential fire thresholds") are too high for some regions, rendering the algorithm unable to detect the (generally) smaller and/or cooler fires characteristic of these regions. In an analysis of small fires in the southeastern United States, for example, Wang et al. (2007), Wang, Qu, Hao, and Liu (2009) found that a large fraction of fire pixels had 4-μm brightness temperatures below the 310 K daytime potential fire threshold used in the Collection 5 algorithm. The authors were able to substantially increase the likelihood of detecting these small fires by reducing the threshold to 293 K, with the stipulation that only those pixels within ≈7 km of smoke (identified automatically using a series of spectral tests) would be considered so as to maintain an acceptable false alarm rate. As part of an evaluation of the MODIS product in the Yucatán Peninsula, Cheng et al. (2013) reported that the "… largest single contributor to the detection omission was the 310 K MODIS 4-μm threshold", and recommended a reduction in the daytime threshold to 305 K for the densely forested areas ubiquitous throughout that region.

While the majority of the above studies emphasized omission errors, it is important to consider commission errors, or false alarms, as well. On this front, the most exhaustive effort to date was that of Schroeder et al. (2008), who validated the Collection 5 Terra MODIS fire product within the Brazilian Amazon using a combination of high resolution Advanced Spaceborne Thermal Emission and Reflection Radiometer (ASTER) and Landsat-7 imagery, airborne data, and ground observations. Among other findings, the authors reported a very high commission error rate (~35%) for the MODIS product associated with small forest clearings within the Brazilian Amazon.

Based on the above findings, and in conjunction with our ongoing quality assessment of and experience with the Collection 5 fire products, we implemented targeted refinements to the MODIS detection algorithm for the Collection 6 reprocessing that commenced in May 2015. Those refinements are described in the next section.

3. Collection 6 algorithm description

The detection algorithm uses native (i.e., unprojected swath) 4-, 11-, and 12-μm brightness temperatures derived from the corresponding 1-km MODIS channels, denoted by T_4, T_{11}, and T_{12}, respectively, and, for daytime observations, 0.65-, 0.86-, and 2.1-μm reflectance (denoted by $\rho_{0.65}$, $\rho_{0.86}$, and $\rho_{2.1}$, respectively), aggregated to 1-kmspatial resolution. Table 1 provides a summary of all MODIS bands used in the algorithm.

The goal of the detection algorithm is to identify "fire pixels" that contain one or more actively burning fires at the time of the satellite overpass. To this end, the algorithm ultimately classifies each pixel of the MODIS swath as *missing data*, *cloud*, *non-fire*, *fire*, or *unknown*. For the sake of backwards compatibility, the Collection 6 fire products actually use a slightly larger set of classes that can be uniquely mapped into the five classes defined here. Framing the algorithm output in terms of these five classes, however, greatly simplifies the subsequent description of the Collection 6 algorithm. Full details may be found in the product User's Guide (Giglio, 2015).

A flowchart of the detection algorithm is shown in Fig. 1. Pixels lacking valid data (e.g., during a calibration maneuver) are summarily assigned to a class of *missing data* and excluded from further consideration.

3.1. Land and water masking

Water, land, and coastal pixels are identified using the updated 1-km land/sea mask contained in the MODIS Collection 6 MOD03/MYD03 geolocation product. Coastal pixels are not processed further by the detection algorithm (aside from being counted) since any residual fragments of unmasked land will usually appear brighter and warmer than the surrounding water, and may easily be mistaken for a small fire. Fig. 2 shows a global sample of fire pixels detected over water during January 2007.

3.2. Cloud masking

While generally adequate, the cloud mask employed in the Collection 5 algorithm occasionally misclassified thick smoke as cloud, thus preventing identification of an otherwise detectable fire. To help alleviate this problem, the fixed thresholds used to mask clouds have been adjusted slightly for Collection 6. Daytime pixels – defined as those having a solar zenith angle less than 85° – are flagged as cloud-obscured (and assigned to the class of *cloud*) if the following combination of conditions is satisfied:

$$(\rho_{0.65} + \rho_{0.86} > 1.2) \text{ or } (T_{12} < 265 \text{ K}) \text{ or}$$
$$(\rho_{0.65} + \rho_{0.86} > 0.7 \text{ and } T_{12} < 285 \text{ K}) \text{ or}$$
$$(\text{water pixel and } \rho_{0.86} > 0.25 \text{ and } T_{12} < 300 \text{ K}).$$

The relaxed thresholds of the new fourth condition, which is applied only to water pixels, exploit the considerable infrared absorption by water. Nighttime pixels are flagged as cloud if the single condition $T_{12} < 265$ K is satisfied. As with earlier versions of the algorithm, these criteria are adequate for identifying larger, cooler clouds, but consistently miss small clouds and cloud edges.

3.3. Identification of potential fire pixels

As with previous versions of the algorithm, a preliminary classification is used to eliminate obvious non-fire pixels. Those pixels not eliminated during this stage are considered to be *potential fire pixels*, and undergo further processing.

A daytime pixel is identified as a potential fire pixel if $T_4 > T_4^*$, $\Delta T > \Delta T^*$ (where $\Delta T \equiv T_4 - T_{11}$), and $\rho_{0.86} < 0.35$ (for nighttime pixels this last condition is dropped). For Collection 5 and earlier, the thresholds T_4^* and ΔT^* were fixed at 310 K (305 K at night) and 10 K, respectively, but for Collection 6 these thresholds are set dynamically for each of the 1354 sample positions of the current MODIS scan (a MODIS scan is composed of 10 lines, each containing 1354 1-km samples, acquired in parallel). This along-scan adjustment helps compensate for local variations in the land surface as well as the systematic increase in atmospheric path length (and hence atmospheric absorption) with scan angle. Dynamically adjusting the potential fire thresholds in this manner was first proposed by Zhukov, Lorenz,

Oertel, Wooster, and Roberts (2006) in the course of developing an active fire detection algorithm for the experimental Bi-spectral Infrared Detection (BIRD) sensor, and subsequently adopted by Wooster, Xu, and Nightingale (2012) in developing a Sentinel-3 Sea and Land Surface Temperature Radiometer (SLSTR) pre-launch active fire product.

Calculation of the thresholds T_4^* and ΔT^* for each MODIS scan proceeds by averaging the values of T_4 and ΔT for all cloud- and glint-free (Section 3.6.1) land pixels within a large, 301-sample by 30-line moving window centered upon sample position j ($0 \leq j \leq 1353$). As the window moves across the scan, a separate T_4 and ΔT average is computed for each sample position; we denote these large-window averages as mean $(T_4)_j$ and mean $(\Delta T)_j$. The fixed dimensions of the large window within "scan space" means that, for nadir pixels, this averaging occurs over an area approximately 306 km $\times$ 30 km in size at the Earth's surface, growing up to approximately 740 km $\times$ 33 km at the edges of the scan.

As a crude means of preventing intense fires from nontrivially biasing the broad-scale averages, pixels having $T_4 > 360$ K (320 K at night) are ignored during averaging. While simplistic, this filtering scheme renders any residual bias negligible, since each average is calculated from a large sample of pixels. In practice, it is rare for more than a few percent of pixels within a window of this size to be true fire pixels.

A potential fire threshold is then independently calculated for each sample position by applying a 5 K offset to the large-window averages. Specifically, $T_4^* = \text{mean}(T_4)_j + 5$ K, with the result constrained so that $300 \text{ K} \leq T_4^* \leq 330 \text{ K}$, and $\Delta T^* = \text{mean }(\Delta T)_j + 5$ K, with the result similarly constrained so that $10 \text{ K} \leq \Delta T^* \leq 35 \text{ K}$. Under this scheme, the two averages required for each sample position will be computed from up to 9030 pixels. Averages based on fewer than 2000 pixels are deemed unreliable, and for such cases the Collection 5 fixed potential fire thresholds are used as a conservative fallback since no reliable information about the large-scale local background is available to the algorithm.

The dynamic thresholds calculated in this step are applied only to land pixels. For water pixels, the more conservative Collection 5 fixed thresholds are used. In addition to recognizing the much smaller variability in surface temperature and emissivity for water, this strategy helps prevent false alarms from occurring in the presence of small, unmasked islands. We will discuss this issue further in Section 3.6.5.

An example of the magnitude of the differences between the Collection 5 and 6 potential fire thresholds for a single 5-min MODIS granule over South America is shown in Fig. 3. In this daytime case, 77% of land pixels had a 4-μm potential-fire brightness temperature threshold below the 310 K fixed value used in the Collection 5 algorithm. In addition, almost every land pixel had a brightness temperature difference threshold (ΔT^*) that exceeded the Collection 5 fixed value of 10 K. The net result for this granule was to reduce the number of potential fire pixels from 49,620 (Collection 5) to 4057 (Collection 6).

We illustrate the impact of the change in potential fire thresholds for Collection 6 using a second example from central Siberia, in which numerous large fires are engulfed in thick

smoke (Fig. 4). The combination of dynamic thermal potential fire thresholds and increased 0.86-μm reflectance threshold produced 95 additional fire pixels associated with large fires, representing an increase of nearly 44% from Collection 5.

3.4. Background characterization

During the subsequent background characterization phase of the algorithm, the radiometric signal of each potential fire pixel in the absence of fire is estimated by computing statistical summaries of neighboring pixels within a small spatial window surrounding the potential fire pixel. The selection of valid background pixels within this moving window (up to 21×21 pixels in size) is described in detail in Giglio et al. (2003), and remains identical for Collection 6, with the important exception that valid background pixels are now restricted to either land *or* water pixels (but never both) to match the land/water state of the potential fire pixel.

In lieu of a detailed description of the local statistics computed for the background window, we provided a summary in Table 2 and refer the reader to Giglio et al. (2003) for additional information. New quantities introduced in Collection 6 include $\bar{L}_4$, the mean 4-μm radiance, $\bar{\rho}_{0.86}$, the mean 0.86-μm reflectance (daytime pixels only), N_c, the number of coast pixels within the background, and N_L, the number of land pixels excluded from the background when the potential fire pixel lies over water.

3.5. Tentative fire detection

In this next phase, the algorithm tentatively identifies pixels containing active fires. For nighttime land pixels, this will in fact be a final identification. For water and daytime land pixels, a subsequent series of rejection tests will be performed, as described in Section 3.6.

As in Collection 5, the algorithm identifies fire pixels (again, tentatively in the case of water and daytime land pixels) by applying a series of absolute and contextual (relative) threshold tests to each potential fire pixel. The absolute threshold criterion of Kaufman et al. (1998) remains unchanged for Collection 6:

$$T_4 > 360 \text{ K} \quad (320 \text{ K at night}). \quad (1)$$

Being deliberately conservative, test (1) provides a direct route by which large and/or particularly intense active fires can be identified. A suite of contextual tests, which offer much greater sensitivity to the much larger proportion of smaller and/or cooler fires, are consequently used to supplement the fixed threshold test. In addition to radiometric information about the potential fire pixel itself, the contextual tests make use of information extracted from the immediate neighborhood, or "background", as described in Section 3.4. These tests, of which there are five, remain unchanged for Collection 6 and are restated here for convenience:

$$\Delta T > \overline{\Delta T} + 3.5 \, \delta_{\Delta T} \quad (2)$$

$$\Delta T > \overline{\Delta T} + 6\,\text{K} \quad (3)$$

$$T_4 > \bar{T}_4 + 3\,\delta_4 \quad (4)$$

$$T_{11} > \bar{T}_{11} + \delta_{11} - 4\,\text{K} \quad (5)$$

$$\delta'_4 > 5\,\text{K} \quad (6)$$

A detailed description of each test may be found in Giglio et al. (2003).

A daytime potential fire pixel is tentatively classified as a fire pixel if either i) test (1) is satisfied, or ii) tests (2) through (4) are satisfied and either test (5) or test (6) is satisfied, otherwise it is classified as a non-fire pixel. A nighttime potential fire pixel is definitively classified as a fire pixel if either i) test (1) is satisfied, or ii) tests (2) through (4) are satisfied, otherwise it is classified as a non-fire pixel.

For potential fire pixels in which background characterization was not possible (because too few valid background pixels were available), only test (1) is applied. If satisfied, the potential fire pixel is tentatively classified as a fire pixel, otherwise it is assigned a final class of *unknown*. In practice, this designation is quite rare. During the five-year period from 2005 through 2009, for example, only 0.001% of all MODIS land pixels (Terra and Aqua combined) were assigned a class of *unknown* in the Collection 5 swath-level fire product.

3.6. Rejection tests

In the final phase of the detection algorithm, pixels tentatively flagged as containing active fires undergo a series of false-alarm rejection tests. These include a *sun-glint rejection test*, applied to both land and water pixels, followed by three tests applied only to tentative land fire pixels: a *desert boundary rejection test*, a *land-pixel coastal rejection test* (formerly referred to unqualifiedly as "coastal rejection"), and a new *forest clearing rejection test*, supplemented with a new *water-pixel coastal rejection test* reserved for tentative fire pixels detected over water. Once all applicable rejection tests have been performed, those tentative fire pixels that remain are definitively classified as *fire*, while those that were at any point rejected are classified as *non-fire*.

3.6.1. Sun glint rejection—The sun glint rejection test remains basically the same for Collection 6, though two angular thresholds were increased to make the test slightly more aggressive in rejecting false alarms, reflecting the fact that the algorithm now seeks to

identify somewhat smaller and/or cooler fires than possible for Collection 5. The tentative fire pixel is rejected if one or more of the following conditions are satisfied:

$$\theta_g < 2° \quad (7)$$

$$\theta_g < 10° \text{ and } \rho_{0.65} > 0.1 \text{ and } \rho_{0.86} > 0.2 \text{ and } \rho_{2.1} > 0.12 \quad (8)$$

$$\theta_g < 15° \text{ and } (N_{aw} + N_w) > 0 \quad (9)$$

Here, N_{aw} is the number of water pixels within the eight pixels surrounding the tentative fire pixel, and θ_g is the angle between vectors pointing in the surface-to-satellite and specular reflection directions (Giglio et al., 2003). Note that test (9) effectively renders the detection of offshore gas flares impossible in the presence of sun glint.

3.6.2. Desert boundary rejection—As discussed by Giglio et al. (2003), the somewhat arbitrary background-fire rejection thresholds employed in the background characterization phase of the algorithm can sometimes produce false alarms in the proximity of surface features that produce a sharp radiometric transition. The specific thresholds used in the MODIS algorithm largely restrict this type of false alarm to the perimeter of hot, arid, and sparsely vegetated or barren regions most commonly associated with deserts. The desert boundary rejection test, which was introduced in Collection 4 to help eliminate such false alarms, remains unchanged for Collection 6. A detailed description of the test can be found in Section 2.2.7 of Giglio et al. (2003).

3.6.3. Land-pixel coastal rejection—When processing a potential fire pixel over land, unmasked water pixels within the background window can depress both $\bar{T}_4$ and $\overline{\Delta T}$, potentially generating a false alarm (Giglio et al., 2003). The land-pixel coastal rejection test, which employs the 0.86- and 2.1-μm reflectance and Normalized Difference Vegetation Index (NDVI) of valid background pixels, is designed to prevent such false alarms. Although originally introduced to help compensate for significant errors that were present in the Collection 4 water mask, we have retained the test in Collection 6 since the distinction between land versus water pixels is inherently ambiguous along coastline. A complete description of the test can be found in Section 2.2.8 of Giglio et al. (2003).

3.6.4. Forest clearing rejection—As noted previously, Schroeder et al. (2008) demonstrated that the MODIS Collection 5 algorithm often misclassifies small (~1-km) tropical forest clearings as fires (Fig. 5). For Collection 6 we have therefore introduced a new rejection test to reduce the frequency of this type of commission error. A daytime fire pixel (land only) is rejected as a false alarm if $T_{11} > \bar{T}_{11} + 3.7\delta_{11}$, $\bar{\rho}_{0.86} > 0.28$, and $T_4 < 325$ K. The first of these three conditions exploits the fact that forest clearings tend to be

significantly warmer than the surrounding intact forest, while the second helps restrict the test to larger patches of tropical forest (which are bright in the near infrared) where a ~1-km clearing might be encountered. The third condition limits the test to fire pixels having a comparatively weak fire signature, which is a consistent property of this type of false alarm. Specific values for the thresholds used in each test were established using reference fire masks derived from 65 ASTER scenes acquired over the Brazilian Amazon that were set aside for training.

3.6.5. Water-pixel coastal rejection—Whereas contamination of the background window with unmasked water pixels can produce a false alarm over land (Section 3.6.3), a similar class of coastal false alarm can occur over water when the potential fire pixel itself is an unmasked land pixel. As a misidentified land pixel, both T_4 and T will be elevated relative to the (generally) cooler water background, to the point that the unmasked land pixel may resemble a small and/or low intensity fire. This scenario is most likely to arise in the vicinity of coastline, where the distinction between land and water pixels is inherently ambiguous. The presence of land or coast pixels in the background window is an obvious indicator for precisely this situation, thus we reject any tentative fire pixel detected over water for which $N_L + N_c > 0$ and test (1) is not satisfied. The additional stipulation with respect to test (1) disables the rejection test in the event the 4-μm signal blatantly exceeds a level that could reasonably be expected for a fire-free land pixel in close proximity to water.

3.7. Fire detection confidence

As with the Collection 4 and Collection 5 algorithms, a heuristic measure of the confidence (C) of each detected fire pixel is calculated as the geometric mean of up to five sub-confidence parameters, designated C_1 through C_5. These parameters are defined in terms of T_4, the number of adjacent water pixels (N_{aw}), the number of adjacent cloud pixels (N_{ac}), the standardized variables $z_4 = (T_4 - \overline{T_4})/\delta_4$ and $z_{\Delta T} = (\Delta T - \overline{\Delta T})/\delta_{\Delta T}$, and the ramp function $S(x;\alpha,\beta)$, defined as

$$S(x; \alpha, \beta) = \begin{cases} 0; & x \leq \alpha \\ (x - \alpha)/(\beta - \alpha); & \alpha < x < \beta \quad (10) \\ 1; & x \geq \beta. \end{cases}$$

Note that our definition differs slightly from (Giglio et al., 2003) in that we have included a minor typographical correction in the bottom inequality. The sub-confidence parameters, which have been adjusted for Collection 6, are defined as follows for daytime fire pixels detected over land:

$$C_1 = S(T_4; T_4^*, 360\,\text{K}) \quad (11)$$

$$C_2 = S(z_4; 3.0, 6) \quad (12)$$

$$C_3 = S(z_{\Delta T}; 3.5, 6) \quad (13)$$

$$C_4 = 1 - S(N_{ac}; 0, 4) \quad (14)$$

$$C_5 = 1 - S(N_{aw}; 0, 4) \quad (15)$$

For nighttime fire pixels, the threshold of 360 K used in the definition of C_1 is reduced to 320 K, and the sub-confidence parameters C_4 and C_5 are not included in the calculation of C. For daytime fire pixels detected over water, C_5 is similarly excluded from the calculation since the presence of adjacent water pixels provides no more information about the quality of the fire detection than the fact that the fire pixel itself lies over water.

3.8. Retrieval of fire radiative power

For Collection 6, the original Kaufman et al. (1998)) empirical fire radiative power (FRP) retrieval has been replaced with the Wooster, Zhukov, and Oertel (2003), Wooster et al. (2012) approach, in which FRP is approximated as

$$\text{FRP} \approx \frac{A_{\text{pix}} \sigma}{a \, \tau_4} (L_4 - \bar{L}_4), \quad (16)$$

where L_4 is the 4-μmradianceof the fire pixel, $\bar{L}_4$ is the 4-μmbackground radiance (Section 3.4), A_{pix} is the area of the MODIS pixel (which varies as a function of scan angle), σ is the Stefan-Boltzmann constant (5.6704×10^{-8} Wm^{-2} K^{-4}), τ_4 is the atmospheric transmittance of the 4-μm channel, and a is a sensor-specific empirical constant. For MODIS, $a = 3.0 \times 10^{-9}$ W m^{-2} sr^{-1} μm^{-1} K^{-4} (Wooster et al., 2003) when radiance is expressed in units of W m^{-2} sr^{-1} μm^{-1}. For the Level 2 (swath) fire product, τ_4 is simply assigned a value of 1, but inclusion of a proper atmospheric correction into some of the higher-level MODIS fire products is under consideration.

The effect of this change in formulation for the Collection 6 product was to consistently decrease FRP for the vast majority of fire pixels (Fig. 6). For the much smaller fraction of comparatively high intensity fire pixels with FRP values that exceed ~500 MW, however, FRP occasionally increased by up to a few percent. The mean FRP of those fire pixels

detected in common was 56.9 MW for Collection 5 compared to 47.7 MW for Collection 6, corresponding to an average decrease of about 16%.

4. Validation

ASTER offers a unique perspective to validate the MOD14 product as it shares the EOS Terra platform with MODIS, providing coincident global imaging over individual 60×60 km scenes acquired along a narrow near-nadir portion ($\pm 8.55°$ in the ASTER short-wave infrared [SWIR] channels) of the 2300 km-wide MODIS swath. ASTER's spatial data characteristics allow sub-pixel validation of MODIS binary fire/no-fire detection data, though are largely inadequate for FRP validation due to frequent pixel saturation (Giglio et al., 2008). Cost considerations compelled by the limited availability of quality reference data have constrained the validation of FRP retrievals to relatively small samples over select areas (e.g. Peterson & Wang, 2013; Schroeder, Oliva, Giglio, & Csiszar, 2014). Other studies built on satellite data inter-comparison analyses to provide additional insight on the consistency of FRP retrievals (e.g. Freeborn, Wooster, Roy, & Cochrane, 2014; Roberts, Wooster, Perry, & Drake, 2005). Because of the outstanding limitations described above, and given the relationship established between FRP retrievals using Collections 5 and 6 data in Section 3.8, we focused on the validation of the fire detection data using the available ASTER reference data.

In order to ensure an unbiased and comprehensive global validation dataset to properly describe the fire detection performance of MOD14, we constructed an equidistant grid composed of approximately 640 cells, each 900 km in diameter (Fig. 7). The data search criteria sought to promote the largest possible range of observation conditions represented in our sample, while achieving reasonable data volume, computer requirements and human resources to effectively complete the analyses. The resulting scene selection process consisted of: [(i)]

i.   Three temporal subsets, namely: 2001–2002, 2003–2004, and 2005–2006;

ii.   Up to three scenes per temporal subset and grid cell showing highest fire activity based on the number of MOD14 fire pixels found within the individual ASTER scene coverage areas. These active fire scenes also included an abundance of fires omitted by the MOD14 product;

iii.   At least one randomly-selected ASTER scene per each temporal subset and grid cell which could include other detected and undetected fires, water bodies, translucent as well as opaque clouds, snow/ice covered surfaces, a fire-free gradient of land surfaces, as well as nighttime data.

The sampling periods in (i) were constrained by data gaps affecting Terra MODIS prior to 2001, and by a sensor malfunction which marked the end of ASTER SWIR channel data acquisitions after May 2007. During our scene selection process, fire-free areas such as open ocean waters, deserts, and polar regions were automatically excluded. A subset of 2466 ASTER scenes (Fig. 7) matching the criteria above was obtained from NASA's Land Processes

Distributed Active Archive Center (LPDAAC). Among those scenes selected, 140 were acquired at night.

The 30-mASTER active fire reference data were derived based on the methodology of Giglio et al. (2008), and consisted of a binary fire/no-fire mask that was co-located with coincident Terra MODIS 1-km data (Csiszar & Schroeder, 2008; Csiszar et al., 2006; Morisette, Giglio, Csiszar, & Justice, 2005; Schroeder et al., 2008). The ASTER fire detection envelope calculated by Giglio et al. (2008) suggests a minimum detectable fire area of approximately 4 m^2 for a typical 900-K flaming fire. Summary fire statistics were derived using the number of 30-m ASTER fire pixels overlapping the effective MODIS pixel footprint, after consideration of the sensor's triangular point spread function in the along-scan direction (Morisette et al., 2005; Schroeder, Csiszar, Giglio, & Schmidt, 2010; Wolfe et al., 2002).

Complementing the data described above, we obtained the corresponding Terra MODIS MOD03 geolocation product from the Land and Atmosphere Archive and Distribution System (LAADS), and the Hansen et al. (2003) MOD44B annual Vegetation Continuous Fields (VCF) gridded product from the LPDAAC. The MOD03 data were used to co-locate all MODIS pixels to the coincident ASTER reference data. The VCF data were used to generate average percentage tree cover estimates in and around each MODIS pixel location using a 20×20 km sampling window, providing broad land cover reference categories to support the global analysis of the MOD14 product performance.

5. Results and discussion

5.1. Global performance

Omission errors were estimated for the entire population using error matrix analysis. In order to estimate the omission error rate as a function of fire size, false negatives were derived as the sum of Terra MODIS pixels showing a number of coincident ASTER fire pixels N without corresponding MOD14 detection, with N varying between 1 and 500. The results were then stratified as a function of percentage tree cover as depicted in Fig. 8. Lower tree cover values (0–20%) were typically associated with grasslands and open savanna, whereas the highest values (>60%) were normally attributed to fires in densely vegetated forest areas. Fires in high tree cover areas were predominantly associated with forest wildfires (e.g., boreal regions) and slash and burn fires (e.g., tropical deforestation) without canopy obstruction. Understory fires in forest areas could not be properly quantified due to low detection rates in both reference and MOD14 data sets.

The overall omission error using fires of all sizes detected by ASTER, which can potentially be as small as 4 m^2 in extent (Giglio et al., 2008), was 86.2%, and less than 10% for reference fires composed of 140 or more ASTER fire pixels. On average, areas of low (<20%) and high (>60%) percentage tree cover showed a 9% absolute difference in omission errors over fire clusters containing less than 100 ASTER pixels. This difference was attributed to lower fire intensity and warmer background conditions increasing the likelihood of MOD14 omission errors in low tree cover areas. Conversely, higher fire intensity and

cooler background conditions reduce the likelihood of a MOD14 omission error in areas of high tree cover.

From Fig. 8 it is apparent that the omission error stabilizes at ~5% for MODIS pixels containing more than ~250 ASTER fire pixels, and remains essentially fixed at this level as fire size continues to increase. We attribute this stabilization to common factors associated with large fires in general. The presence of large burn scars adjacent to the active fire line, for example, can affect the background characterization, potentially reducing the spatial and/or radiometric contrast with the fire pixel and thus the efficacy of the contextual tests. Variable plume and atmospheric properties can also lead to partial or complete obscuration of the fire signal, thereby affecting the ability of the algorithm to detect some parts of a large fire.

For comparative purposes, Fig. 8 also shows the corresponding omission error curves derived for the MOD14 Collection 5 product. Relative to the previous product version, MOD14 Collection 6 showed noticeable improvement in detection performance of large fire clusters (>300 ASTER pixels) occurring in areas with percentage tree cover greater than 60%. The difference was mainly associated with MODIS pixels in boreal forest regions where thick smoke from large wildfires either exceeded the lower 0.86-μmpotential fire threshold used for Collection 5, or triggered the more liberal Collection 5 cloud screening, leading to higher omission errors.

Commission errors (false alarms) were defined as MOD14 pixels without coincident ASTER reference fire activity. All potential false alarms were visually inspected, and MOD14 pixels showing ASTER fire activity in the immediate vicinity (neighboring pixels) were classified as true positives in order to account for any unresolved pixel spatial response and/or co-location errors. Additionally, MOD14 pixels associated with industrial heat sources (e.g., steel mills) were not counted as commission errors given that those recurring pixels can be readily isolated from the rest using simple detection persistence analysis (e.g., Schroeder et al., 2008). Finally, all confirmed false alarms were inspected for the presence of radiometrically distinct burn scars in order to separate false alarms in areas completely free of biomass burning from those associated with recent activity.

Fig. 9 shows the global commission-error rates for MOD14 Collections 5 and 6. False alarm rates were divided into two subsets describing pixels with and without coincident burn scars. Both data sets showed a strong dependency on the percentage tree cover, with higher false alarm rates in areas dominated by dense woody vegetation. This feature is corroborated by previous results and is explained by the occurrence of land clearings that induce high thermal contrast with the cooler forest background, thereby mimicking the spectral signature of an actual vegetation fire (Schroeder et al., 2008). Most importantly, the MOD14 Collection 6 product showed a significant reduction in false alarm rates compared to Collection 5 over high tree cover regions. This improvement in performance is a result of the forest clearing rejection test described in Section 3.6.4. Overall, the MOD14 Collection 6 daytime global commission error was 1.2%, compared to 2.4% in Collection 5. We found no evidence of commission errors in the nighttime data analyzed, which included 838 MOD14 fire pixels among ~500,000 MODIS night pixels sampled. We therefore conclude that false

alarms in the MOD14 data are constrained to daytime data when differential solar reflection and heating can sometimes lead to ambiguous classification of land surface pixels.

5.2. Regional performance

To assess algorithm performance regionally, we partitioned our validation results into the 14 Global Fire Emissions Database (GFED) regions used in numerous earlier studies (Fig. 10). As before, we consider both omission and commission errors, now expressing the former in terms of the complementary probability of detection widely used in earlier fire-product validation studies (e.g. Morisette et al., 2005, Schroeder et al., 2008).

Collection 6 detection probabilities showed significant regional variability, ranging from a minimum of 7% in the Middle East (MIDE) to a maximum of 26% in Australia and New Zealand (AUST). Compared to Collection 5, the probability of detection for the Collection 6 product exhibited a ~3% absolute increase in Boreal North America and Boreal Asia, a ~1% absolute increase in Equatorial Asia and Central Asia, a ~1% absolute decrease in NH South America, and little or no change in the remaining nine regions.

Not unexpectedly, the observed variability in the probability of detection was strongly driven by regional differences in fire size (Fig. 11). For all regions, fire size (in terms of 30-m ASTER fire pixels) was extremely skewed toward small fires, more or less following an exponential distribution (Fig. 12). The presence of a comparatively small number of very large fires in the tail of each distribution generally renders the arithmetic mean highly biased toward large fires, to a great extent ignoring the contribution of the much larger population of small fires, hence we summarize the "typical" fire size within each region in terms of the median.

Regional commission error rates are shown in Fig. 13. For the Collection 6 product, significant absolute decreases of ~5% occurred in both Equatorial Asia and SH South America. More modest reductions (~1% absolute) were observed for Central Asia, NH South America, and Temperate North America, and in the remaining cases the Collection 6 commission error rate remained effectively the same or increased only negligibly.

6. Conclusions

We have described improvements in the MODIS active fire detection algorithm, and the associated MOD14 and MYD14 fire products, as part of the MODIS Collection 6 land-product reprocessing activity. The Collection 6 algorithm is intended to address limitations observed with the previous Collection 5 fire product, notably the occurrence of false alarms arising from small forest clearings, and the omission of large fires obscured by thick smoke. Processing was expanded to oceans and other large water bodies to facilitate monitoring of offshore gas flaring. Additionally, fire radiative power is now retrieved using the Wooster et al. (2003, 2012) radiance approach. This change resulted in a consistent decrease in FRP for the vast majority of fire pixels, but with occasional slight increases (by up to a few percent) for the much smaller fraction of comparatively high intensity fire pixels.

We performed a Stage-3 validation of the Collection 5 and Collection 6 Terra MODIS fire products using reference fire maps derived from more than 2500 high-resolution ASTER images. Our results indicated targeted improvements in the performance of the Collection 6 active fire detection algorithm compared to Collection 5, with reduced omission errors (i.e., an increased probability of detection) over large fires, and reduced false alarm rates in tropical ecosystems. Overall, the MOD14 Collection 6 daytime global commission error was 1.2%, compared to 2.4% in Collection 5. Broken down regionally, the probability of detection for the Collection 6 product exhibited a ~3% absolute increase in Boreal North America and Boreal Asia, a ~1% absolute increase in Equatorial Asia and Central Asia, a ~1% absolute decrease in NH South America, and little or no change in the remaining nine GFED regions. Not unexpectedly, the observed variability in the probability of detection was strongly driven by regional differences in fire size. Overall, there was a net positive change in Collection 6 algorithm performance globally.

The Collection 6 algorithm is now run as part of the MODIS land-product forward processing stream, as well as the operational Land Atmosphere Near Real-time Capability for EOS (LANCE) system. The entire MODIS archive has been reprocessed and is now freely available from the USGS/NASA Land Processes Distributed Active Archive Center (https://lpdaac.usgs.gov/). As we have noted previously, operation of the Terra MODIS sensor from launch through October 2000 was problematic, rendering the MODIS fire product for this time period of limited utility. Consequently, time series analyses of MODIS fire data should be restricted to observations acquired from November 2000 onward.

The MODIS Collection 6 algorithm and product has also been used as the baseline for the forthcoming science-quality Suomi National Polar-orbiting Partnership (S-NPP) Visible Infrared Imaging Radiometer Suite (VIIRS) 750-mactive fire product to be produced by NASA (Csiszar et al., 2014).

Acknowledgments

References

Bromley L. Relating violence to MODIS fire detections in Darfur, Sudan. International Journal of Remote Sensing. 2010; 31:2277–2292. DOI: 10.1080/01431160902953909

Chen Y, Velicogna I, Famiglietti JS, Randerson JT. Satellite observations of terrestrial water storage provide early warning information about drought and fire season severity in the Amazon. Journal of Geophysical Research: Biogeosciences. 2013; 118:495–504. DOI: 10.1002/jgrg.20046

Cheng D, Rogan J, Schneider L, Cochrane M. Evaluating MODIS active fire products in subtropical Yucatán forest. Remote Sensing Letters. 2013; 4:455–464. DOI: 10.1080/2150704X.2012.749360

Chuvieco E, Giglio L, Justice CO. Global characterization of fire activity: towards defining fire regimes from earth observation data. Global Change Biology. 2008; 14:1488–1502. DOI: 10.1111/j.1365-2486.2008.01585.x

Csiszar I, Schroeder W. Short-term observation of the temporal development of active fires from consecutive same-day ETM + and ASTER imagery in the Amazon: implications for active fire product validation. IEEE Journal of Selected Topics in Applied Earth Observations and Remote Sensing. 2008; 1:248–253.

Csiszar I, Morisette J, Giglio L. Validation of active fire detection from moderate resolution satellite sensors: the MODIS example in Northern Eurasia. IEEE Transactions on Geoscience and Remote Sensing. 2006; 44:1757–1764.

Csiszar I, Schroeder W, Giglio L, Ellicott E, Vadrevu KP, Justice CO, Wind B. Active fires from the Suomi NPP visible infrared imaging radiometer suite: product status and first evaluation results. Journal of Geophysical Research: Atmospheres. 2014; 119:803–816. DOI: 10.1002/2013JD020453

Freeborn PH, Wooster MJ, Roberts G. Addressing the spatiotemporal sampling design of MODIS to provide estimates of the fire radiative energy emitted from Africa. Remote Sensing of Environment. 2010; 115:475–498. DOI: 10.1016/j.rse.2010.09.017

Freeborn PH, Wooster MJ, Roy DP, Cochrane MA. Quantification of MODIS fire radiative power (FRP) measurement uncertainty for use in satellite-based active fire characterization and biomass burning estimation. Geophysical Research Letters. 2014; 141:1988–1994. DOI: 10.1002/2013GL059086

Giglio L. Technical Report. University of Maryland; 2015. MODIS collection 6 active fire product user's guide, revision A. (URL: http://modisfire.umd.edu/files/MODIS_C6_Fire_User_Guide_A.pdf)

Giglio L, Csiszar I, Restás A, Morisette JT, Schroeder W, Morton D, Justice CO. Active fire detection and characterization with the advanced spaceborne thermal emission and reflection radiometer (ASTER). Remote Sensing of Environment. 2008; 112:3055–3063. DOI: 10.1016/j.rse.2008.03.003

Giglio L, Descloitres J, Justice CO, Kaufman YJ. An enhanced contextual fire detection algorithm for MODIS. Remote Sensing of Environment. 2003; 87:273–282.

Giglio L, Randerson JT, van der Werf GR, Kasibhatla PS, Collatz GJ, Morton DC, Defries RS. Assessing variability and long-term trends in burned area by merging multiple satellite fire products. Biogeosciences. 2010; 7:1171–1186. DOI: 10.5194/bg-7-1171-2010

Hansen MC, DeFries RS, Townshend JRG, Carroll M, Dimiceli C, Sohlberg RA. Global percent tree cover at a spatial resolution of 500 meters: first results of the MODIS vegetation continuous fields algorithm. Earth Interactions. 2003; 7doi: 10.1175/1087-3562

Hantson S, Padilla M, Corti D, Chuvieco E. Strengths and weaknesses of MODIS hotspots to characterize global fire occurrence. Remote Sensing of Environment. 2013; 131:152–159. DOI: 10.1016/j.rse.2012.12.004

Hawbaker TJ, Radeloff VC, Syphard AD, Zhu Z, Stewart SI. Detection rates of the MODIS active fire product in the United States. Remote Sensing of Environment. 2008; 112:2656–2664. DOI: 10.1016/j.rse.2007.12.008

He L, Li Z. Enhancement of a fire-detection algorithm by eliminating solar contamination effects and atmospheric path radiance: application to MODIS data. International Journal of Remote Sensing. 2011; 32:6273–6293. DOI: 10.1080/01431161.2010.508057

Ichoku C, Kaufman YJ. A method to derive smoke emission rates from MODIS fire radiative energy measurements. IEEE Transactions on Geoscience and Remote Sensing. 2005; 43:2636–2649.

Justice CO, Townshend JRG, Vermote EF, Masuoka E, Wolfe RE, Saleous N, … Morisette J. An overview of MODIS land data processing and product status. Remote Sensing of Environment. 2002; 83:3–15.

Kaiser JW, Heil A, Andreae MO, Benedetti A, Chubarova N, Jones L, … van der Werf GR. Biomass burning emissions estimated with a global fire assimilation system based on observed fire radiative power. Biogeosciences. 2012; 9:527–554. DOI: 10.5194/bg-9-527-2012

Kaufman YJ, Justice CO, Flynn LP, Kendall JD, Prins EM, Giglio L, … Setzer AW. Potential global fire monitoring from EOS-MODIS. Journal of Geophysical Research. 1998; 103:32215–32238.

de Klerk H. A pragmatic assessment of the usefulness of the MODIS (Terra and Aqua) 1-km active fire (MOD14A2 and MYD14A2) products for mapping fires in the fynbos biome. International Journal of Wildland Fire. 2008; 17:166–178.

Koren I, Remer LA, Longo K. Reversal of trend of biomass burning in the Amazon. Geophysical Research Letters. 2007; 34:L20404.doi: 10.1029/2007GL031530

Longo KM, Freitas SR, Andreae MO, Setzer A, Prins E, Artaxo P. The coupled aerosol and tracer transport model to the Brazilian developments on the regional atmospheric modeling system

(CATT-BRAMS) — part 2: model sensitivity to the biomass burning inventories. Atmospheric Chemistry and Physics. 2010; 10:5785–5795. DOI: 10.5194/acp-10-5785-2010

Maier SW, Russell-Smith J, Edwards AC, Yates CJ. Sensitivity of the MODIS fire detection algorithm (MOD14) in the savanna region of the Northern Territory, Australia. ISPRS Journal of Photogrammetry and Remote Sensing. 2013; 76:11–16.

McCarty J, Justice CO, Korontzi S. Agricultural burning in the Southeastern United States detected by MODIS. Remote Sensing of Environment. 2007; 108:151–162. DOI: 10.1016/j.rse.2006.03.020

Mollicone D, Eva HD, Achard F. Human role in Russian wild fires. Nature. 2006; 440

Morisette JT, Giglio L, Csiszar I, Justice CO. Validation of the MODIS active fire product over southern Africa with ASTER data. International Journal of Remote Sensing. 2005; 26:4239–4264.

Peterson D, Wang J. A sub-pixel-based calculation of the fire radiative power from MODIS observations: 2. Sensitivity analysis and potential fire weather application. Remote Sensing of Environment. 2013; 129:231–249. DOI: 10.1016/j.rse.2012.10.020

Peterson D, Hyer E, Wang J. Quantifying the potential for high-altitude smoke injection in the North American boreal forest using the standard MODIS fire products and subpixel-based methods. Journal of Geophysical Research: Atmospheres. 2014; 119:3401–3419. DOI: 10.1002/2013JD021067

Reid JS, Hyer EJ, Prins EM, Westphal DL, Zhang J, Wang J, … Hoffman JP. Global monitoring and forecasting of biomass-burning smoke: description of and lessons from the fire locating and modeling of burning emissions (FLAMBE) program. IEEE Journal of Selected Topics in Applied Earth Observations and Remote Sensing. 2009; 2:144–162. DOI: 10.1109/JSTARS.2009.2027443

Ressl R, Lopez G, Cruz I, Colditz RR, Schmidt M, Ressl S, Jiménez R. Operational active fire mapping and burnt area identification applicable to Mexican nature protection areas using MODIS and NOAA-AVHRR direct readout data. Remote Sensing of Environment. 2009; 113:1113–1126. DOI: 10.1016/j.rse.2008.10.016

Roberts G, Wooster MJ, Perry GLW, Drake N. Retrieval of biomass combustion rates and totals from fire radiative power observations: application to southern Africa using geostationary SEVIRI imagery. Journal of Geophysical Research. 2005; 110:D21111.doi: 10.1029/2005JD006018

Schroeder W, Csiszar I, Giglio L, Schmidt CC. On the use of fire radiative power, area, and temperature estimates to characterize biomass burning via moderate to coarse spatial resolution remote sensing data in the Brazilian Amazon. Journal of Geophysical Research. 2010; 115:D21121.doi: 10.1029/2009JD013769

Schroeder W, Giglio L, Aravéquia JA. Comment on 'Reversal of trend of biomass burning in the Amazon' by Ilan Koren, Lorraine A. Remer, and Karla Longo. Geophysical Research Letters. 2009; 36:L03806.doi: 10.1029/2008GL035659

Schroeder W, Oliva P, Giglio L, Csiszar IA. The new VIIRS 375 m active fire detection data product: algorithm description and initial assessment. Remote Sensing of Environment. 2014; 143:85–96. DOI: 10.1016/j.rse.2013.12.008

Schroeder W, Prins E, Giglio L, Csiszar I, Schmidt C, Morisette JT, Morton D. Validation of GOES and MODIS active fire detection products using ASTER and ETM + data. Remote Sensing of Environment. 2008; 112:2711–2726.

Sofiev M, Vankevich R, Lotjonen M, Prank M, Petukhov V, Ermakova T, … Kukkonen JJ. An operational system for the assimilation of the satellite information on wild-land fires for the needs of air quality modelling and forecasting. Atmospheric Chemistry and Physics. 2009; 9:6833–6847. DOI: 10.5194/acp-9-6833-2009

Tanpipat V, Honda K, Nuchaiya P. MODIS hotspot validation over Thailand. Remote Sensing. 2009; 1:1043–1054. DOI: 10.3390/rs1041043

Vadrevu KP, Ellicott E, Giglio L, Badarinath KVS, Vermote E, Justice CO, Lau WKM. Vegetation fires in the himalayan region — aerosol load, black carbon emissions and smoke plume heights. Atmospheric Environment. 2012; 47:241–251. DOI: 10.1016/j.atmosenv.2011.11.009

Wang W, Qu JJ, Hao X, Liu Y. Analysis of the moderate resolution imaging spectroradiometer contextual algorithm for small fire detection. Journal of Applied Remote Sensing. 2009; 3:031502.doi: 10.1117/1.3078426

Wang W, Qu JJ, Hao X, Liu Y, Sommers WT. An improved algorithm for small and cool fire detection using MODIS data: A preliminary study in the Southeastern United States. Remote Sensing of Environment. 2007; 108:163–170. DOI: 10.1016/j.rse.2006.11.2009

Wiedinmyer C, Akagi SK, Yokelson RJ, Emmons LK, Al-Saadi JA, Orlando JJ, Soja AJ. The fire INventory from NCAR (FINN): a high resolution global model to estimate the emissions from open burning. Geoscientific Model Development. 2011; 4:625–641. DOI: 10.5194/gmd-4-625-2011

Wolfe RE, Nishihama M, Fleig AJ, Kuyper JA, Roy DP, Storey JC, Patt FS. Achieving sub-pixel geolocation accuracy in support of MODIS land science. Remote Sensing of Environment. 2002; 83:31–49.

Wooster MJ, Zhang YH. Boreal forest fires burn less intensely in Russia than in North America. Geophysical Research Letters. 2004; 31:L20505.doi: 10.1029/2004GL020805

Wooster M, Xu W, Nightingale T. Sentinel-3 SLSTR active fire detection and FRP product: pre-launch algorithm development and performance evaluation using MODIS and ASTER datasets. Remote Sensing of Environment. 2012; 120:236–254. DOI: 10.1016/j.rse.2011.09.033

Wooster MJ, Zhukov B, Oertel D. Fire radiative energy for quantitative study of biomass burning: derivation from the BIRD experimental satellite and comparison to MODIS fire products. Remote Sensing of Environment. 2003; 86:83–107.

Zhukov B, Lorenz E, Oertel D, Wooster M, Roberts G. Spaceborne detection and characterization of fires during the bi-spectral infrared detection (BIRD) experimental small satellite mission (2001–2004). Remote Sensing of Environment. 2006; 100:29–51. DOI: 10.1016/j.rse.2005.09.019
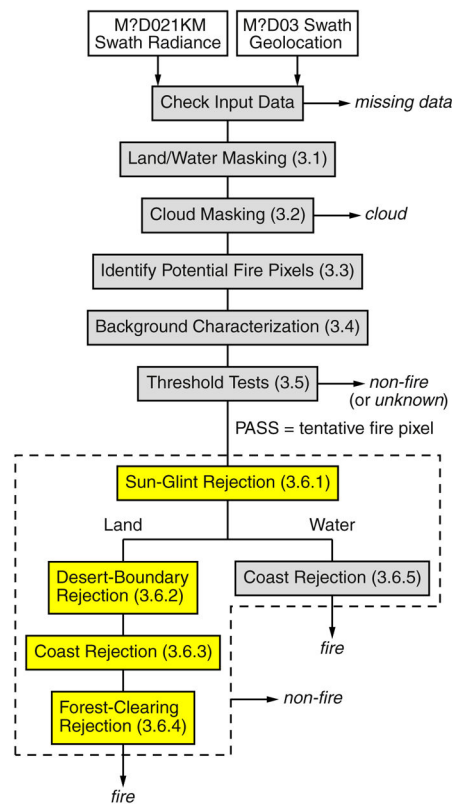
Fig. 1.
Flowchart of Collection 6 detection algorithm, with possible output classes signified by italicized text. Grey boxes indicate algorithm steps performed for both daytime and nighttime pixels, while yellow boxes show steps restricted to daytime pixels. The individual rejection tests described in Section 3.6 are shown inside the dashed box; those tentative fire pixels failing any rejection test are summarily classified as *non-fire*. Failure of the threshold tests (center box) applied to potential fire pixels will produce an output class of *non-fire*, or in those very rare cases when background characterization was not possible, *unknown*.
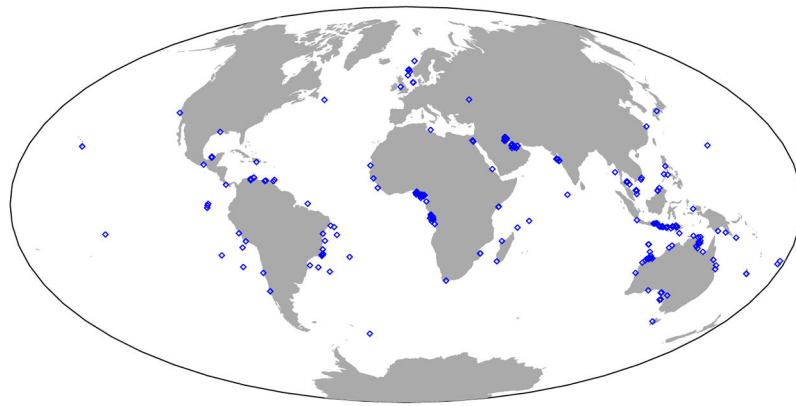
Fig. 2.
Locations of all Collection 6 Terra and Aqua MODIS fire pixels detected over water during January 2007.
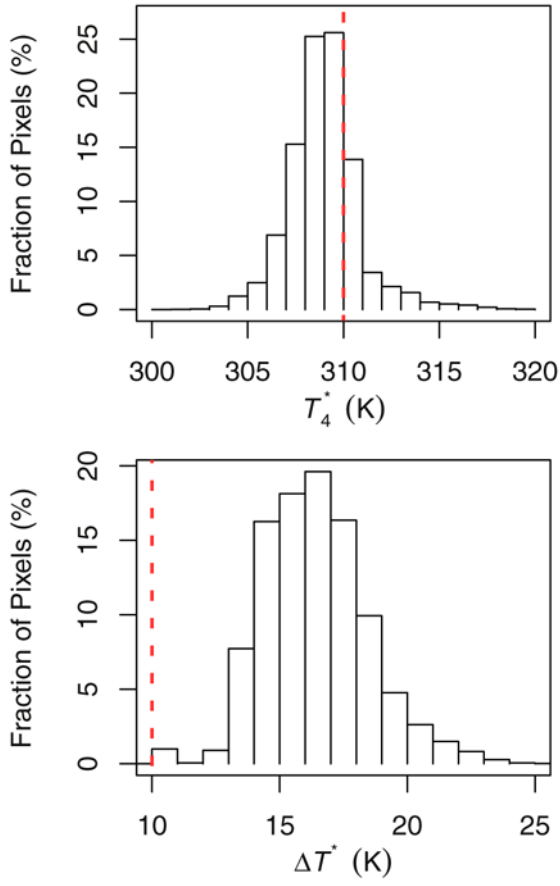
Fig. 3.

Distribution of Collection 6 dynamic potential fire thresholds T_4^* (top panel) and T^* (bottom panel) used for the Terra MODIS granule acquired on 5 March 2003 at 14:15 UTC over South America. For this daytime granule, 77% of land pixels had a 4-μm potential-fire brightness temperature threshold (T_4^*) below the 310 K fixed threshold (red dashed line in top panel) used in the Collection 5 algorithm, and nearly all land pixels had a brightness-temperature difference threshold (T^*) above the 10-K fixed threshold (red dashed line in bottom panel) used in Collection 5.
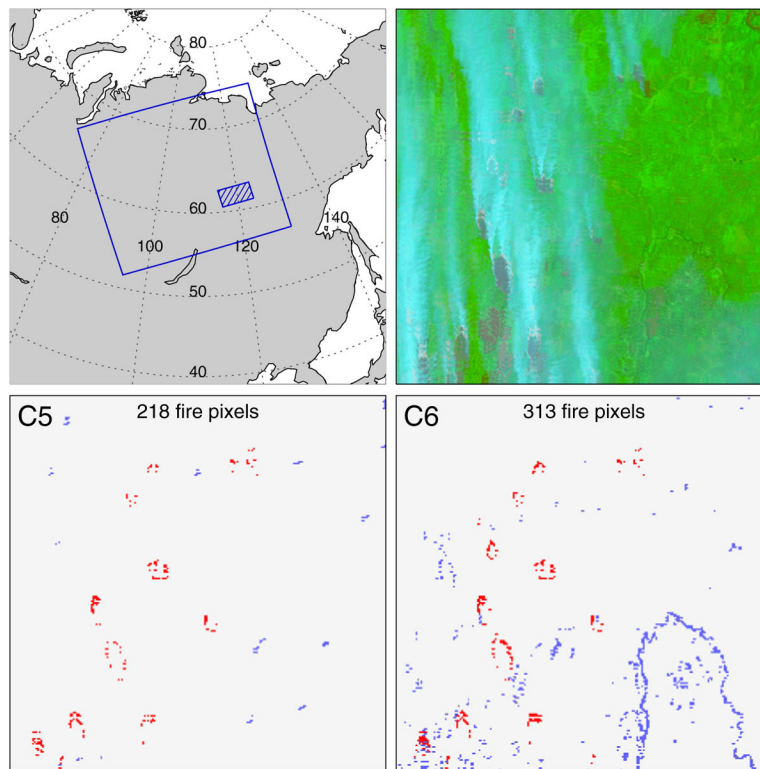
Fig. 4.

Example of smoke-obscured fire fronts mapped in the Collection 5 (lower left) and Collection 6 (lower right)MODIS fire product for the 5-min Aqua granule acquired over northern Russia on 22 July 2014 at 05:20 UTC. In both bottom panels, fire pixels are shown in red, water pixels in light blue, and non-fire land pixels in light grey. The edges of the MODIS swath from which this example was extracted are outlined in blue in the top left panel, with the smaller shaded rectangular region indicating the subset of the swath shown in the remaining panels. The upper right panel shows a false-color composite of the same subset generated from MODIS bands 7, 2, and 1. In this representation, active flaming fronts have a pale red color, smoke appears pale blue, vegetation appears green, and recently burned areas appear dark grey. The size of the off-nadir swath subset shown in the top right and bottom panels is approximately 426 km in the along-scan (horizontal) direction and 226 km in the along-track (vertical) direction.
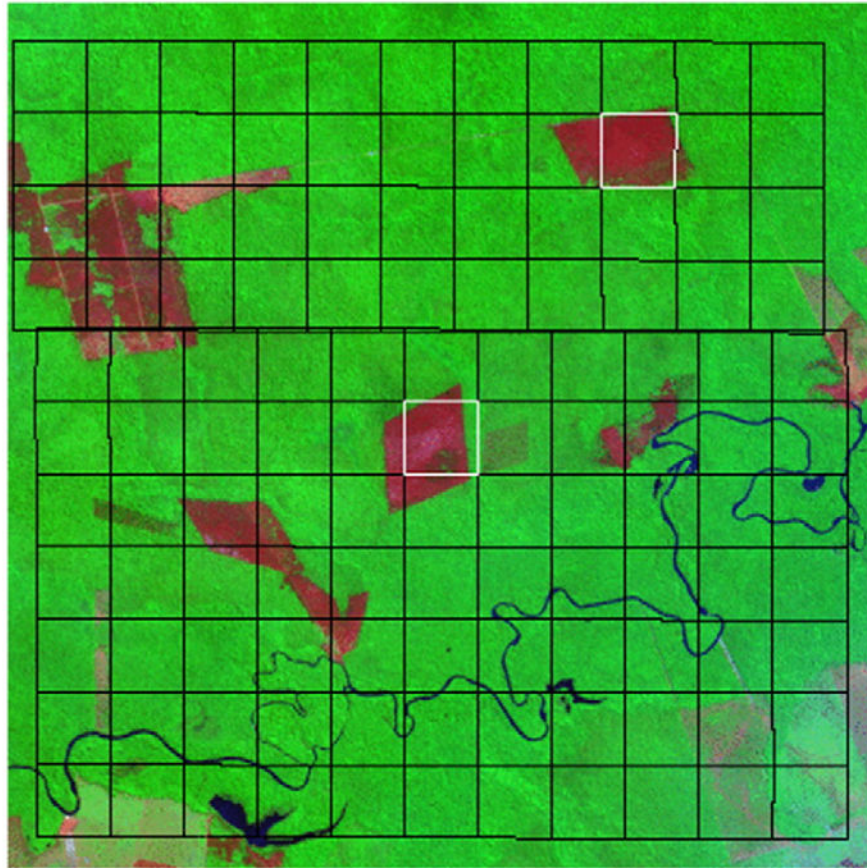
Fig. 5.
False color ASTER image of forest clearings in Pará, Brazil, acquired on 19 August 2005 at 13:59 UTC illustrating false alarms in the Collection 5 product, with ASTER bands 8 (2.33 μm) shown as red, 3 N (0.82 μm) shown as green, and 1 (0.56 μm) shown as blue. The approximate edges of the 1-km Terra MODIS pixels are outlined in black, with the two pixels incorrectly flagged as encompassing fires outlined in white. Neither false fire pixel appears in the Collection 6 product. The center of this scene is located at 6.489°S, 52.716°W.
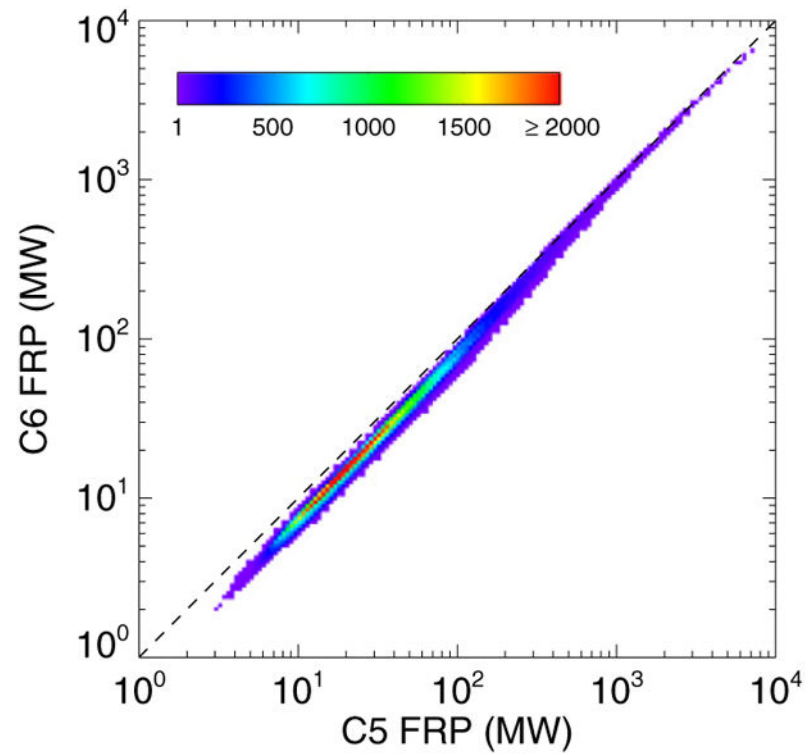
Fig. 6.
Collection 6 (C6) versus Collection 5 (C5) fire radiative power (FRP) for approximately 240,000 Terra and Aqua MODIS fire pixels detected globally from 1 to 10 August 2005. The color scale indicates the number of points within each element of a 200×200 grid that partitions the two-dimensional space bounded by the axes.
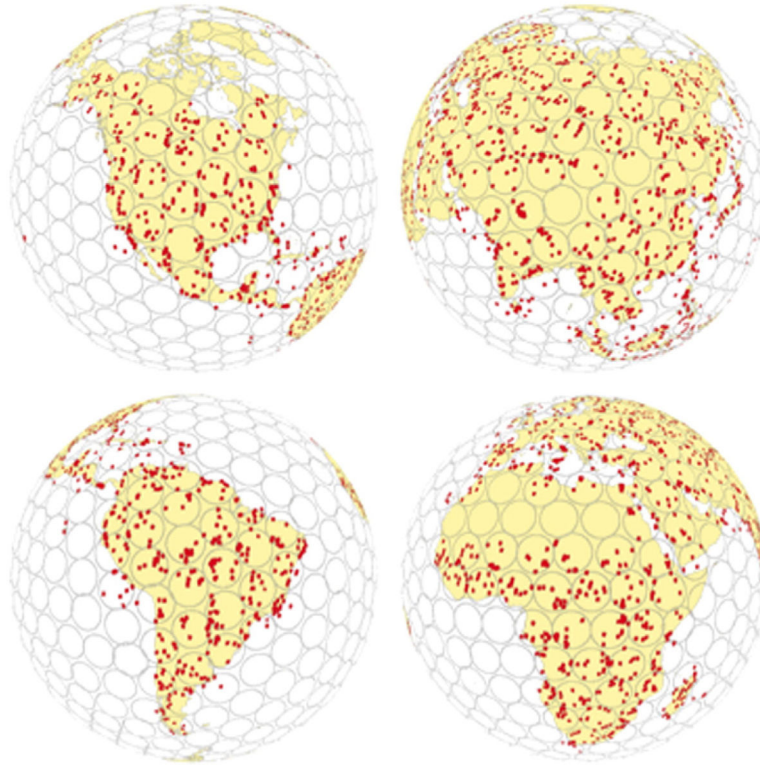
Fig. 7.
Global equidistant 900 km resolution sampling grid and the distribution of individual 60 × 60 km ASTER reference scenes (red shade) used to validate the near-nadir 1-km Terra MODIS fire product.
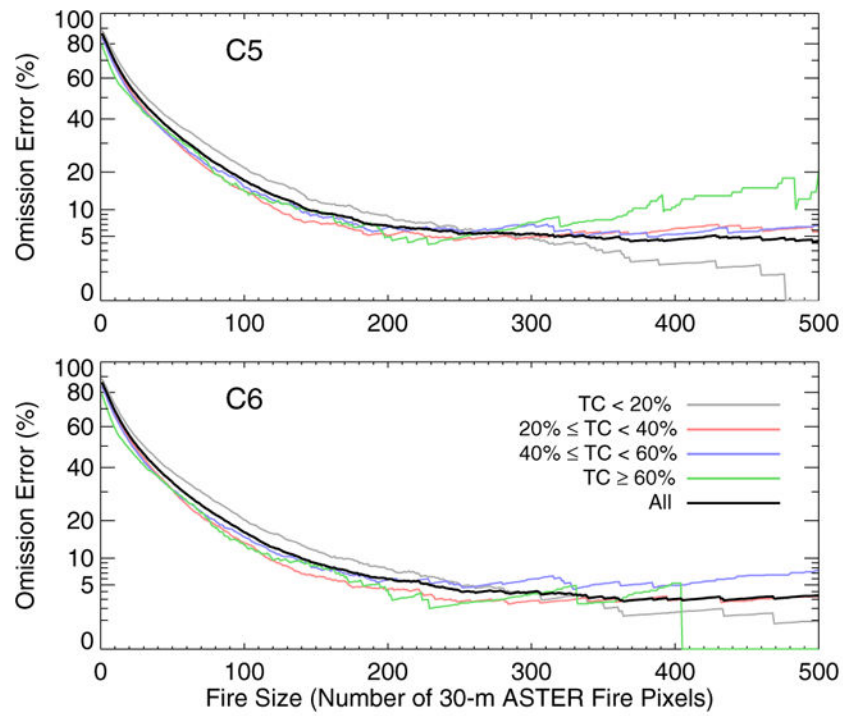
Fig. 8.
Overall omission error rates for MOD14 Collection 5 (top) and Collection 6 (bottom) products (black curves), and partitioned by percentage tree cover (TC). Note the nonlinear vertical axes.
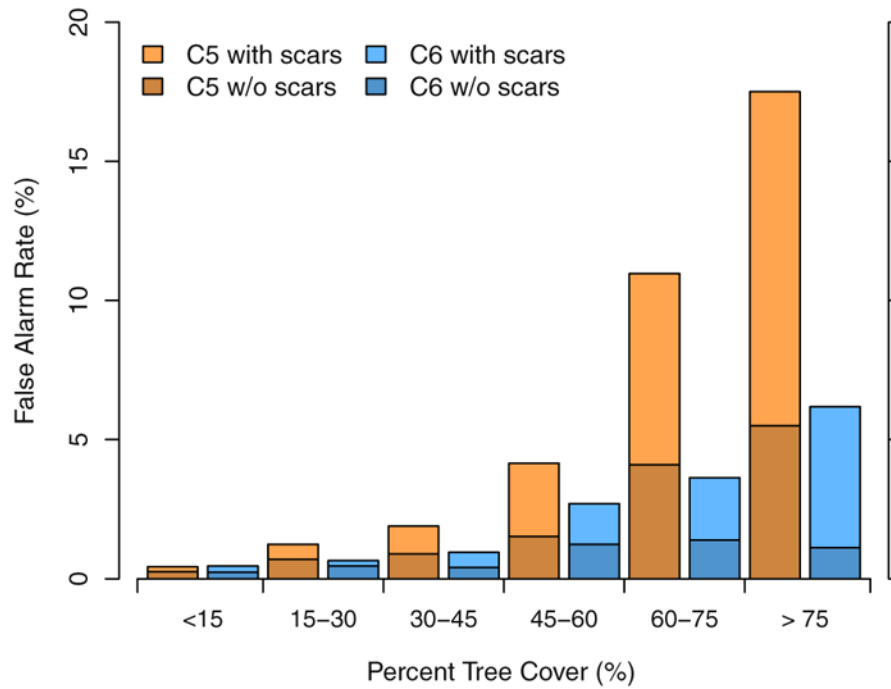
Fig. 9.
False alarm rates derived for MOD14 Collections 5 (orange) and 6 (blue) as a function of fractional tree cover. False alarm rates are divided into pixels with and without associated burn scars.

BONA	Boreal North America	NHAF	Northern Hemisphere Africa
TENA	Temperate North America	SHAF	Southern Hemisphere Africa
CEAM	Central America	BOAS	Boreal Asia
NHSA	Northern Hemisphere South America	CEAS	Central Asia
SHSA	Southern Hemisphere South America	SEAS	Southeast Asia
EURO	Europe	EQAS	Equatorial Asia
MIDE	Middle East	AUST	Australia and New Zealand

Fig. 10.
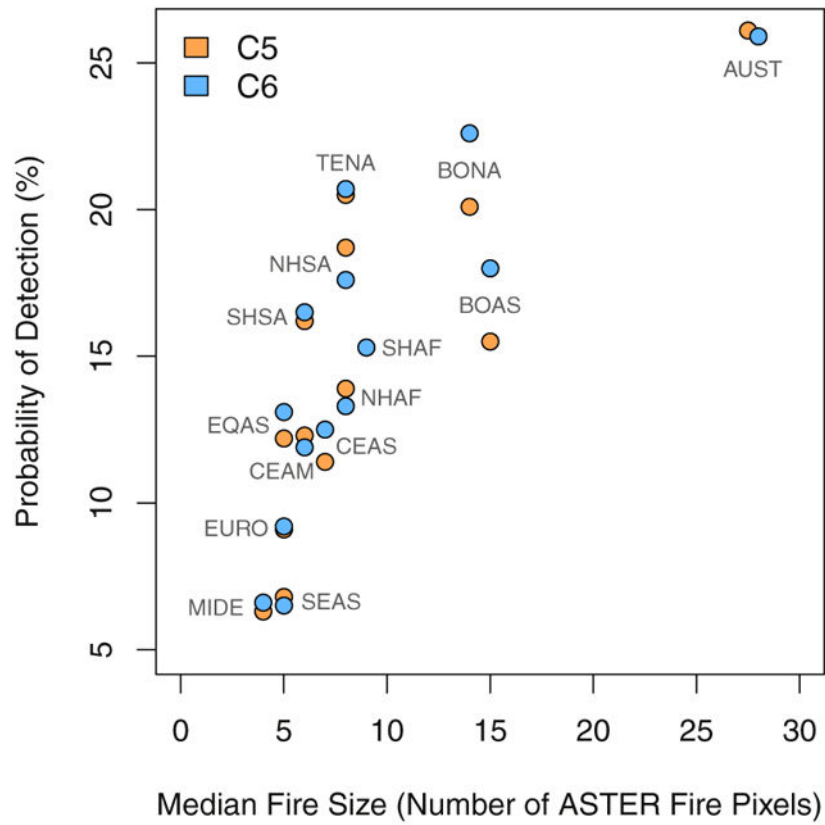Map of the 14 GFED regions, after Giglio et al. (2010).

Fig. 11.
Regional detection probabilities for MOD14 Collection 5 (orange dots) and Collection 6 (blue dots) as a function of the median number of 30-m ASTER fire pixels within a 1-km MODIS pixel.
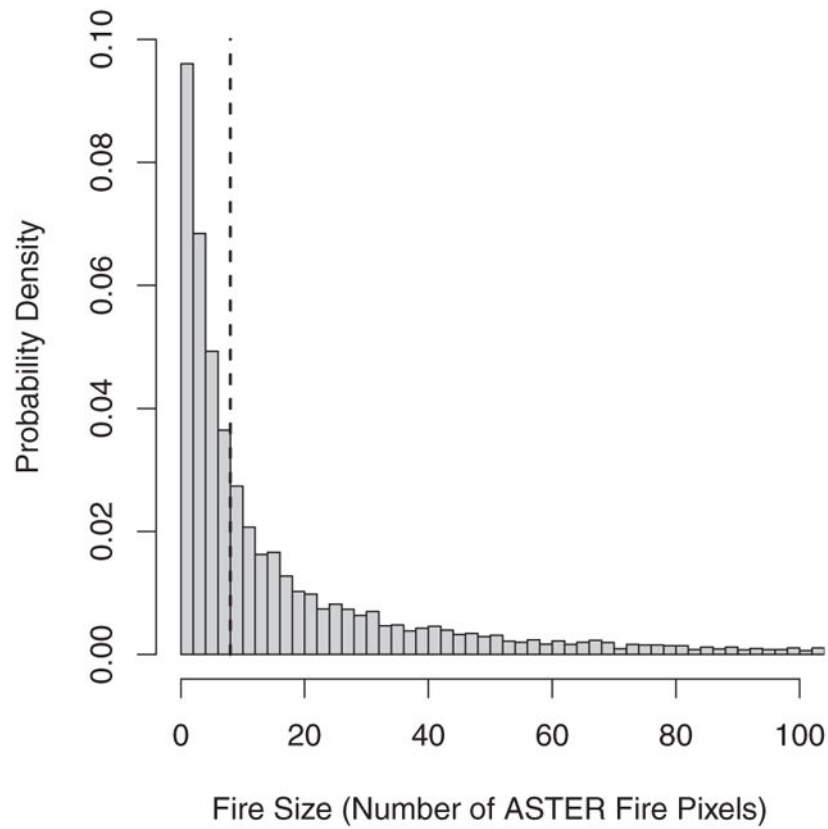
Fig. 12.
Representative distribution of fire sizes as determined with ASTER, i.e., the number of 30-mASTER fire pixels within a 1-km MODIS pixel, for the NH Africa region. For clarity, the plot truncates the distribution at just over 100 ASTER fire pixels; in actuality the right tail of the distribution extends well beyond 1000 ASTER fire pixels due to a handful of extreme cases. The dashed vertical line marks the location of the median of the distribution.
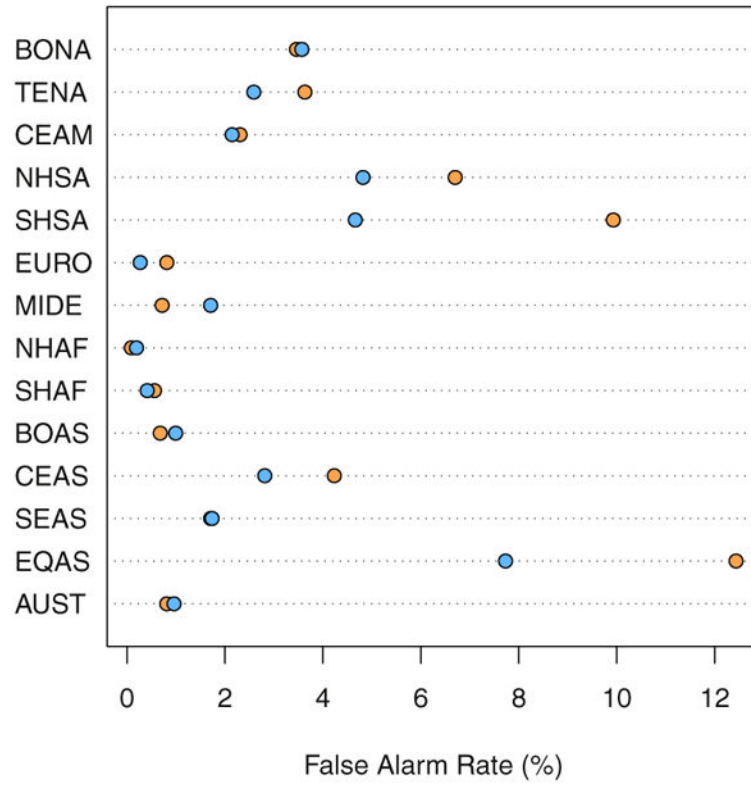
Fig. 13.
Regional commission error (false alarm) rates for MOD14 Collection 5 (orange dots) and Collection 6 (blue dots).

Table 1

Summary of MODIS channels used in the detection algorithm and ingested from the Collection 6 MODIS Level-1B radiance product (MOD021KM/MYD021KM). Details regarding the blending of bands 21 and 22 may be found in Giglio, Descloitres, Justice, and Kaufman (2003).

Channel number	Central wavelength (μm)	Purpose
1	0.65	Sun glint and coastal false alarm rejection; cloud masking.
2	0.86	Bright surface, sun glint, and coastal false alarm rejection; cloud masking.
7	2.1	Sun glint and coastal false alarm rejection.
21	4.0	High-range channel for active fire detection.
22	4.0	Low-range channel for active fire detection.
31	11.0	Active fire detection, cloud masking, forest clearing rejection.
32	12.0	Cloud masking.

Table 2

Statistical quantities computed for contextual window. The acronym MAD denotes the mean absolute deviation. More detailed descriptions can be found in Giglio et al. (2003).

Variable	Description
$\bar{L}_4$	Mean 4-μm radiance.
$\bar{T}_4$	Mean 4-μm brightness temperature.
$\bar{T}_{11}$	Mean 11-μm brightness temperature.
$\overline{\Delta T}$	Mean brightness temperature difference ($\equiv T_4 - T_{11}$).
δ_4	4-μm brightness temperature MAD.
δ_{11}	11-μm brightness temperature MAD.
δ_T	Brightness temperature difference MAD.
N_v	Number of valid pixels within contextual window.
$\bar{\rho}_{0.86}$	Mean 0.86-μm reflectance (daytime pixels only).
$\bar{T}'_4$	Mean 4-μm brightness temperature of pixels rejected as background fires.
δ'_4	4-μm brightness temperature MAD of pixels rejected as background fires.
N_f	Number of pixels within contextual window rejected as background fires.
N_c	Number of coast pixels (always excluded) within the contextual window.
N_w	Number of excluded water pixels within the contextual window.
N_L	Number of excluded land pixels within the contextual window.